JOURNAL OF AIRCRAFT
Vol. 37, No. 4, July–August 2000

Aerodynamic Characteristics of Spanwise Cambered Delta Wings

Lance W. Traub*
Texas A&M University, College Station, Texas 77843-3141

A wind-tunnel investigation was undertaken to determine the effect of various spanwise camber distributions on the aerodynamic characteristics of a 75-deg delta wing. Data presented include force balance, seven-hole probe survey, as well as surface flow visualization and vortex burst trajectories. The experimental results indicate that some of the tested dihedral and anhedral geometric variations can augment lift significantly, requiring only minor modifications to the planar wing geometry to implement. It was found that anhedral generally promotes lift augmentation compared to the basic wing, whereas dihedral has the opposite effect. Anhedral and dihedral have the greatest effect when applied near the wing tips, with anhedral enhancing lift through an increase in strength of both the primary and secondary wing leading-edge vortices. Nonplanarity had a small effect on the vortex burst characteristics.

Nomenclature

b	= wing span
C_D	= drag coefficient
C_L	= lift coefficient
C_m	= pitching moment coefficient
C_{pt}	= maximum stagnation pressure loss
c_r	= wing root chord
k	= wing efficiency parameter
k_P	= potential lift constant
p	= height of wing tip/semispan
q	= freestream dynamic pressure
r	= radial coordinate, measured from vortex centerline
s	= local semispan
U	= freestream velocity
V_A	= axial velocity
V_θ	= rotational velocity
x, y, z	= Cartesian coordinates
α	= wing centerline incidence
Γ	= vortex circulation
Λ	= wing leading-edge sweep angle
ϕ	= wing dihedral angle, defined (−) for anhedral and (+) for dihedral
ω	= axial vorticity

Subscripts

k	= kink
max	= maximum
min	= minimum
np	= nonplanar
pr	= projected

Introduction

SINCE the first investigation of a delta wing in the 1930s,[1] a vast pool of knowledge has evolved on the behavior of this class of wings. Sharp-edged deltas are associated with unique flow physics, embodied in the conical leading-edge vortices that form from the shear layer generated by merging of the upper and lower surface leading-edge outflow boundary layers. The vortices, depending on the slenderness of the delta wing, characterize the flowfield, and augment lift through high induced surface velocities. The augmented lift, vortex lift, is stable until approximately 25–35 deg, for slender delta wings ($\Lambda > 70$ deg). Unfortunately, this lift augmentation is at the expense of high drag, as the vortex lift is associated with loss of leading-edge suction, or partial suction for blunt-edged delta wings. Delta wings are poor lift generators due to their low aspect ratio[2] [$\mathrm{d}C_L/\mathrm{d}\alpha \approx 4\tan^{0.8}(90\ \mathrm{deg} - \Lambda)$], thus making enforced leading flow separation and consequent vortex formation an attractive (but potentially costly in terms of drag) mechanism for lift enhancement.

Improvement of the performance of delta wings has revolved around either reducing their drag through the application of passive devices, or increasing their lift through active applications, for example, blowing. Passive devices invariably encompass some form of leading-edge camber, optimally variable. The best example of this type of device is the leading-edge vortex flap[3,4] (LEVF), which works by concentrating the suction of the leading-edge vortex on the flap, so that when the flap is deflected below the plane of the wing, the vortex-induced loading can oppose drag. Lift augmentation has usually encompassed some form of blowing, either spanwise or chordwise along the vortex core. Significant lift augmentation can be achieved through blowing at moderate to high lift coefficients. Depending on the jet's orientation, lift may be augmented either through the jet increasing the axial momentum of the vortex, thereby delaying breakdown, or by the jet acting as a low-pressure sink, drawing the vortex closer to the wing surface. However, blowing has the added complexity of requiring ducting and involves loss of engine power through the bleeding of air. Combining along the core blowing with a LEVF on a 60-deg delta wing–body has shown significant lift augmentation with concurrent drag reduction.[5] The use of a trailing-edge Gurney flap on a delta wing[6] has resulted in significant lift augmentation, with an increase of lift-to-drag ratio (L/D) at moderate to high C_L, the small scale of the Gurney flap causing little drag penalty. All of these studies, however, are concerned with the effect on performance of relatively localized wing modifications. They do not examine the effects of gross planform changes on the wing's behavior.

For a planar wing with a constrained span, Munk[7] has shown that the minimum induced drag occurs when the downwash in the wake is constant; the wing has elliptic spanwise loading. The downward impulse of the wake flow is proportional to the lift, and the kinetic energy of the flow is proportional to the induced drag. Consequently, for minimum drag, the wing should have a large span to capture as great a volume of air as possible, thus requiring less work to accelerate it downward to generate the lift impulse.

For nonplanar systems, Munk[7] has shown that induced drag is a minimum when the component of the induced velocity normal to the lifting line is proportional to the cosine of the angle of inclination of that element. If the wing is not constrained to be planar, Cone[8] and Lowson[9] have shown that numerous nonplanar wing forms (wings

Received 12 July 1999; revision received 4 February 2000; accepted for publication 7 February 2000. Copyright © 2000 by Lance W. Traub. Published by the American Institute of Aeronautics and Astronautics, Inc., with permission.

*Postdoctoral Research Associate, Aerospace Engineering Department. Associate Member AIAA.

with spanwise camber of their lifting lines, end plates, etc.) can improve efficiency beyond the theoretical planar minimum. Nonplanarity affects the aerodynamics of the wing in several ways. The curve of the spanwise bound vortex results in an incremental induced velocity parallel to the freestream, so-called induced lift. This effect is asymmetric with respect to anhedral or dihedral. Cone[8] shows that to reduce the induced drag, the strength of the trailing vorticity should be minimized and the lifting elements should be distributed over a large area. For a planar wing, this may be achieved by increasing the wing span for a given lift coefficient and by distributing the trailing vorticity over a large vertical area for a nonplanar system. The underlying principle is that by spreading the vorticity for a given lift, a larger mass of air is affected and, consequently, the velocity at a point is lowered so by reducing the wake velocities.

The studies of Lowson[9] and Cone[8] show that nonplanarity for high-aspect-ratio wings is most beneficial when applied near the wing tips, with an end plate showing the greatest efficiency. The drag of the wing end-plate combination is theoretically reduced by the upwash induced on the wing by the end plate, reducing the induced α and associated vortex drag of the wing. Experimental studies have generally not realized these performance gains due to the increased profile and interference drag of the end plate.

To date, research efforts focused on performance improvement of delta wings through nonplanarity implemented through spanwise camber have been virtually nonexistent. Most studies of delta wings have involved either some form of localized leading-edge camber (e.g., LEVFs) or a combination of chordwise and spanwise camber (conical camber).[10] An exception is the experimental investigation by Squire.[11] Squire's test cases consisted of a $\Lambda = 76$-deg wing ($AR = 1$) with various leading-edge droop angles and spanwise shoulder locations. Significant in his study was the inclusion of a delta wing with pure anhedral of 16.7 deg, such that the wing possessed no chordwise camber. Squire's results showed that leading-edge camber increases the lift curve slope of the wing above the attachment incidence but shifts the angle of attack for zero lift to a positive value. An exception to this was the result for the delta with pure anhedral. As this wing had no chordwise camber, the angle of attack for zero lift occurred at $\alpha = 0$ deg. The results exhibited a substantial increase in lift beyond that for the projected planar wing, with an increase in lift of 11% at $\alpha = 16$ deg.

Experimental studies of dihedral on swept wings have been primarily concerned with stability effects.[12,13] Washburn and Gloss[14] investigated the effects on vortex breakdown of circular arc spanwise camber on a 76-deg delta wing. Their results indicated that for this wing planform and camber distribution, anhedral and dihedral had an insignificant effect on the vortex and its burst location. A subsequent study by Washburn and Gloss[15] focused on the effects of anhedral and dihedral on the longitudinal and lateral characteristics of a supersonic cruise configuration. Their results show that for the configuration studied (which resembled a cranked arrow wing), longitudinal forces where relatively invariant, with the anhedral model showing a slight lift improvement. Lateral data was similar for all of the model variations. A study has been conducted on the effects of winglets on a delta wing as described by Smith and Campbell.[16]

The logical application of the delta wing configuration is in the supersonic regime, following from its low wave drag. As reported by Polhamus,[17] vortex lift exists for a Mach number greater than 1. In supersonic flight, increasing the Mach number reduces the magnitude of the vortex lift developed until the leading-edge stagnation point approaches the wing's leading edge (i.e., the leading edge becomes supersonic), at which point the upwash ahead of the wing tends to zero and so, consequently, does the vortex lift. Increasing the wing's AR also reduces the quantity of vortex lift developed. Traub[18] has shown that spanwise camber can be interpreted as an increase (dihedral) or decrease (anhedral) in effective wing sweep. By analogy, it may be surmised that, for the present wings, configurations with an anhedral panel may experience a localized decrease in vortex lift (vice versa for dihedral) in the supersonic regime.

The results presented in this study are part of a larger research effort[19] on the effects of spanwise camber, which was motivated by the lack of a systematic investigation of the effects of pure spanwise camber on delta wings. In this paper, all of the tested planforms had a projected leading-edge sweep angle of 75 deg. Various spanwise camber distributions were evaluated, with data for constant camber (a $\wedge$ or $\vee$ wing) and inboard and outboard spanwise camber presented. In all cases, the magnitude of the nonplanarity (i.e., the vertical displacement of the wing tip from the wing centerline divided by the semispan) was constant and equal to 0.27. The effect of the location of the kink or shoulder where the wing was bent, for a given amount of nonplanarity (i.e., the wing tip height/semispan) was investigated to determine if slender wings benefitted mostly from outboard camber as per high AR wings, or if the fundamentally different flow mechanism on delta wings requires an alternative camber distribution to be effective. The present investigation includes force balance measurements, on and off surface flow visualization (vortex burst trajectories), as well as flowfield surveys using a seven-hole probe.

Experimental Equipment and Procedure

Figure 1a shows geometric details of the models used in the study. Figure 1b presents details of the model mount. All of the wings were fabricated from a thin mild steel plate. Wentz and Kohlman[20] have shown that for thin wings (thickness/$c_r = 1.1\%$) a square wing leading edge shows similar performance characteristics to a chamfered or bevelled leading edge. Consequently, to eliminate the necessity of bevelling the wing's leading edges, they were manufactured from 1.52-mm-thick steel plate. The wing's thickness, combined with a root chord of 375 mm, yields a thickness-to-chord ratio of 0.41%. A projected leading-edge sweep angle of 75 deg was investigated. For each wing, the projected span (201 mm) and, consequently, the AR (1.07), was constrained and, thus, the arc length of the wing was variable. This is in accordance with the work of Cone,[8] who has shown that in comparing planar and nonplanar wings, the use of the projected AR is appropriate. The magnitude of the nonplanarity (wing tip height/semispan) was equal for all wings, and was =0.27 to match that of a constant anhedral/dihedral delta (a $\wedge$ or $\vee$ wing) with $\phi = \pm 15$ deg. Spanwise camber variations encompassed inboard and outboard camber, with $2y_k/b = \frac{1}{3}$ and $\frac{2}{3}$ (Fig. 1a). The wings were tested normal and inverted to yield anhedral and dihedral.

The wings were attached to a mount that consisted of a thin reinforcing spine that extended for 203 mm along the root chord of the wing, so as to minimize wing flexing. No spanwise or chordwise deformation of the wings was observed during any of the tests. The model dimensions were kept to a minimum to reduce the effect of the wind-tunnel walls. Tests were undertaken in Texas A&M University's 3×4 ft continuous wind tunnel at $U = 45$ m/s and $Re = 1.14 \times 10^6$ based on c_r, unless mentioned otherwise.

Vortex burst trajectories were determined in Texas A&M University's 2×3 ft water tunnel. These tests were run at a freestream velocity of 0.4 m/s yielding a root chord Reynolds number of 0.15×10^6. Spanwise distance markers were drawn on the upper wing surface, allowing determination of the vortex burst location to within $\approx 1\%$ of the wing root chord. Dye was injected at the wing apex so as to best elucidate the leading-edge vortices. Video footage was recorded during the tests and analyzed subsequently to determine the trajectories. The spiral vortex breakdown mode was seen to predominate. The location of breakdown was taken as that at which the vortex core filament showed the distinctive kink associated with this mode.

A six-component Aerolab sting balance was used for force and moment determination. The accuracy of this balance is estimated to be 0.5% of the maximum measured for lift, drag, and pitching moment. Balance resolution is better than 2×10^{-4} of the measured coefficient on all channels. Through repeated data runs, repeatability of the balance for lift, drag, and pitching moment is estimated at $\Delta C_L = 0.0008$, $\Delta C_D = 0.0005$, and $\Delta C_m = 0.0008$. Model angle of attack can be set to within 0.05 deg. Force balance data, as well as tunnel dynamic pressure, were acquired using a personal computer equipped with a 16-bit A/D board. A dedicated data acquisition program for this force balance samples each data channel at 1000 times and averages it. The data acquisition code also displays graphically,

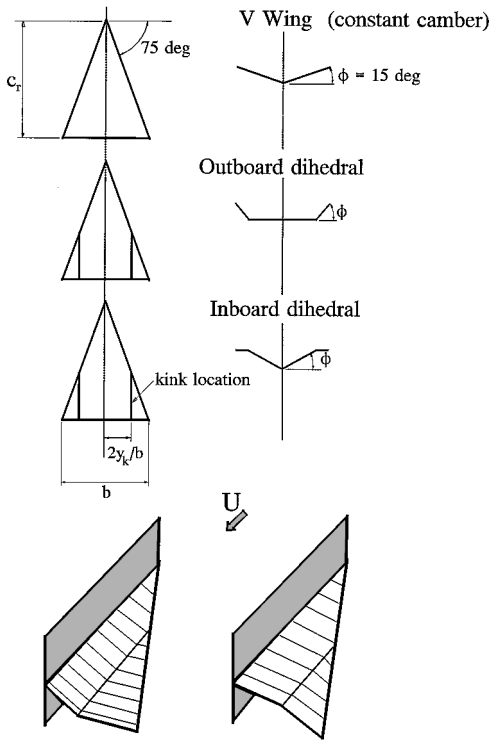

a) Wind-tunnel model details

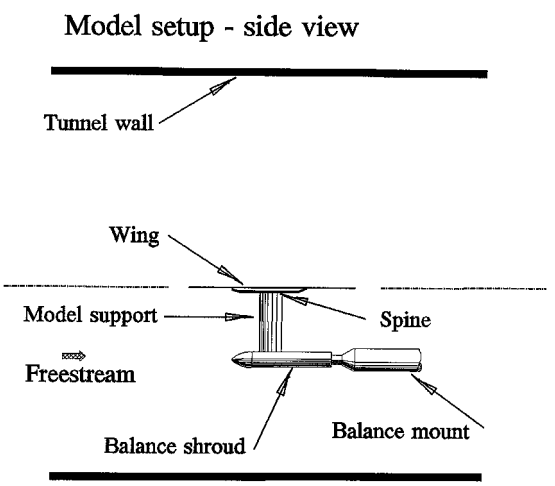

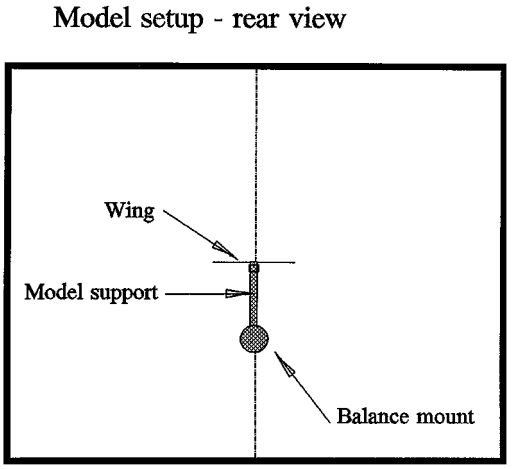

b) Model mounting details

Fig. 1 Experimental equipment.

in real time, lift, drag, and pitching moment, such that erroneous data can be recognized instantly.

The force balance tests comprised pitching the model through a set angle-of-attack range from −2 to 56 deg. Data were recorded at 2-deg intervals. In the vicinity of the maximum lift coefficient, smaller α increments were used where necessary. Pitching moment was taken about 0.25 of the wing's projected mean aerodynamic chord, effectively the wing mid-root chord. The moment reference length was the mean aerodynamic chord.

The presence of the wind-tunnel model support results in a tare drag, as well as interference between the support and the model and the model and the support. Tare and interference were determined using an image system[21] because this method is relatively simple to implement and yields the total interference and tare effects and may additionally be used to determine the wind-tunnel flow angularity. The effect of the model support on pitching moment was determined similarly. The flow angularity was calculated to be 0.76 deg at a freestream velocity of 46 m/s. This angularity includes effects due to balance and test section misalignment, as well as tunnel flow angularity. In this study, solid and wake blockage were corrected for using the method of Shindo.[22] Upwash corrections were applied using the method detailed in Ref. 21. Due to equipment limitations, it was necessary to run the flowfield surveys at a freestream velocity of 20 m/s, yielding a Reynolds number of 0.5×10^6 based on the wing's centerline root chord. A 1.6-mm-diam, seven-hole conical probe was used for the surveys. The probe was moved using a three-component traversing mechanism. The accuracy of this system in positioning is within 0.03 mm. Pressures measured by the probe were evaluated using a 32-channel electronic scanning pressure (ESP) pressure sensor with a measurement range of ±2.5 kPa. Calibration of the ESP was checked by sequentially comparing a reference pressure imposed on each channel against the value measured by a calibrated Air Neotronics micromanometer. Agreement between the micromanometer and the ESP was generally within 1%. Prior to each test the ESP was zeroed to reduce drift. After completing a test, the ESP was checked to ascertain if the zeros had drifted significantly. The pressures measured by the ESP were digitized using a 12-bit A/D board. The probe was calibrated using a least-squares calibration routine. The accuracy of the calibration was verified by inclining the probe at various pitch and yaw angles and comparing the predicted and set angles. Consequently, the accuracy of the probe calibration is estimated to be within 0.5 deg at a yaw or pitch angle of 30 deg. Comparisons of axial velocity recorded with the seven-hole probe and a pitot tube at a similar location in the tunnel showed agreement within 0.5% at a freestream velocity of 20 m/s.

The camber distributions that showed favorable performance characteristics compared to the planar wing were surveyed using the seven-hole probe to determine the effect of the nonplanarity on the flow physics. At a chordwise station to be surveyed, a 30×35 grid was used yielding 1050 points in the crossflow plane. The grids extended laterally from 0.2 to 1.2 of the local semispan. For all cases the grids extended vertically to 0.7 of the local semispan. The lower circuit bound of the probe was 3 mm from the wing surface to eliminate any possibility of contact due to flexing of the support members and to reduce interference between the probe and the upper wing surface. The spanwise resolution of the grids was 0.029 and the vertical resolution 0.023 of the local semispan. The wings were surveyed at $x/c_r = 0.3$, 0.5, 0.7, and 0.9 to determine the chordwise effects of ϕ on the flowfield. At each grid data point in the flowfield, the pressures were sampled 120 times and averaged. After moving to a new point in the flowfield, data measurement was delayed for 3 s to allow the pressures to stabilize. All data were acquired using the AeroView® data acquisition and analysis code. The surveys were undertaken at $\alpha = 20$ deg, with the probe tracing a rectangular section perpendicular to the wing surface.

AeroView was used for processing data from the probe surveys. This included calculation of vorticity and circulation. The code allows the evaluation of circulation using either a surface integral of the vorticity or a line integral of the velocity around a contour enclosing the surface. The total crossflow circulation was evaluated using both of these methods for all of the surveyed data, and in no case

was the discrepancy greater than 1.5% (near the vortex core) and was typically <0.2%. This was encouraging as it would be expected that circulation based on vorticity integration may incur a somewhat greater error due to differentiation of the discrete velocity field. It was, thus, assumed that the level of uncertainty in the measurement of circulation may be satisfactorily evaluated by determining the uncertainty in the line integral method for determining Γ. Evaluation of various data sets yielded an uncertainty in the measurement of circulation of 0.76%.

Results and Discussion

Wentz and Kohlman[20] conducted a comprehensive force balance investigation of the effects of wing sweep on a range of planar delta wings. The results of Ref. 20 have been used to verify numerous theoretical/computational methodologies. Figure 2 shows comparisons between the present results and those of Wentz and Kohlman[20] for a planar 75-deg sweep delta wing. Agreement between the data sets is seen to be excellent. Figure 2 also shows a repeated data run for the $2y_k/b = \frac{2}{3}$, outboard cambered, anhedral configuration.

Figures 3 and 4 present the effect of anhedral/dihedral and spanwise camber location on lift coefficient. For both data sets the effect

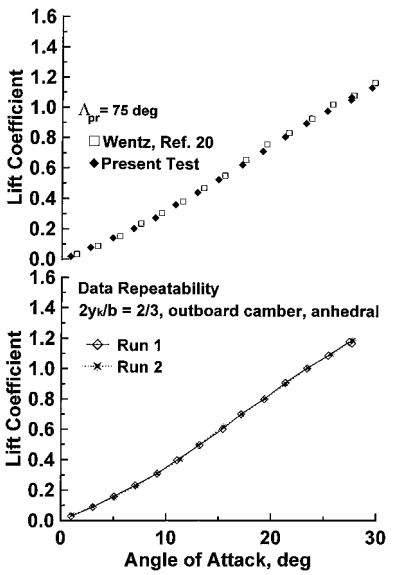

Fig. 2 Data repeatability and comparison with results of Wentz and Kohlman.[20]

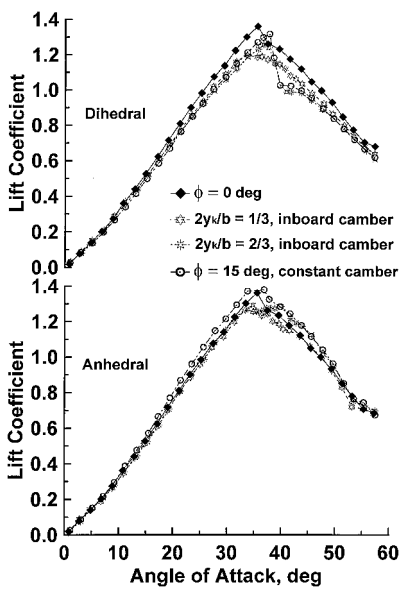

Fig. 3 Effect of inboard camber on measured lift coefficient.

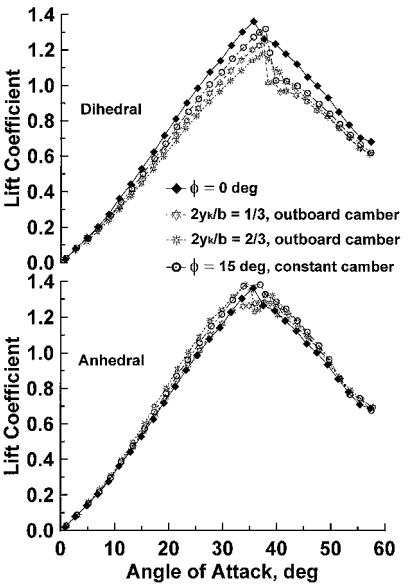

Fig. 4 Effect of outboard camber on measured lift coefficient.

of anhedral and dihedral is equivalent at low lift coefficients, suggesting that the impact of ϕ on the attached flow lift curve slope is weak. Inboard camber effects for $p = 0.27$ are shown in Fig. 3. Data for $\phi = \pm 15$ deg is included in Fig. 3 because this wing has a similar level of nonplanarity p to the inboard and outboard cambered wings. For the constant spanwise cambered wing, $\phi = \pm 15$ deg, anhedral increases lift compared to the planar wing for $\alpha > 10$ deg, whereas dihedral has the opposite effect. For the inboard spanwise camber variations evaluated, this form of spanwise camber (either anhedral or dihedral) does not enhance lift for $C_L < C_{L\max}$ for either $2y_k/b = \frac{1}{3}$ or $\frac{2}{3}$, which show similar performance. The most obvious effect of inboard camber is in lift behavior around $C_{L\max}$ in Fig. 3. In Fig. 3, $2y_k/b = \frac{2}{3}$ in the anhedral orientation results in a flat $C_{L\max}$ region, whereas $2y_k/b = \frac{1}{3}$, dihedral, results in a docile stall compared to $\phi = 0$ deg.

Data for the outboard camber are displayed in Fig. 4. Behavior of $2y_k/b = \frac{2}{3}$ is notable in that it generates the largest lift increase relative to the planar wing of any tested anhedral variation and the largest lift decrement with the wing inverted, that is, spanwise dihedral. This outboard cambered wing ($2y_k/b = \frac{2}{3}$) recorded lift increments of 7 and 9% compared to the planar wing at $\alpha = 15$ and 25 deg, respectively. This lift augmentation is also significant considering the limited wing modification embodied in the configuration. Note that the most effective tested implementation of nonplanarity for these slender wings mimics the optimal distribution near the wing tips for high AR wings. Nonetheless, the underlying flow mechanisms responsible for the lift augmentation are, most likely, quite different. The outboard cambered ($2y_k/b = \frac{2}{3}$, anhedral) wing also displays peculiar poststall behavior (Fig. 4), exhibiting a second, smaller C_L peak. With $2y_k/b = 1/3$, outboard camber, anhedral demonstrates similar $C_{L\max}$ behavior to that seen with inboard camber and anhedral, that is, a docile stall.

Wing efficiency may be gauged in terms of $k = \pi AR\, C_D/C_L^2$, which, for this class of wings, is given by $k = \pi AR \tan\alpha/C_L$. Thus, for a given AR and α, efficiency can only be improved through an increase in lifting ability. For a constrained span unswept planar wing, k has a theoretical minimum value of unity.[7] For nonplanar wings however, the value of k may be appreciably lower.[8] For slender delta wings, k typically reduces as α increases due to increased lift from the vortex sheets. Inboard camber is seen to generally degrade k compared to a wing with constant anhedral (Fig. 5). Outboard anhedral camber with $2y_k/b = \frac{2}{3}$ (Fig. 6) yields greater efficiency (lower k) than for any other tested variation, suggesting that outboard camber may be the most effective means of implementing anhedral for this configuration.

The effect of spanwise camber on pitching moment is presented in Figs. 7 and 8. Pitchup (an abrupt change or slope reversal of the

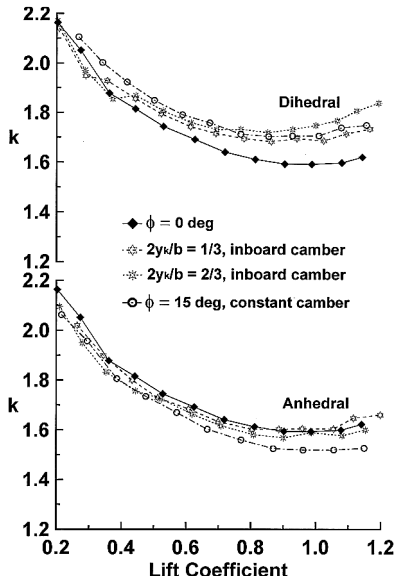

Fig. 5 Effect of inboard camber on induced efficiency.

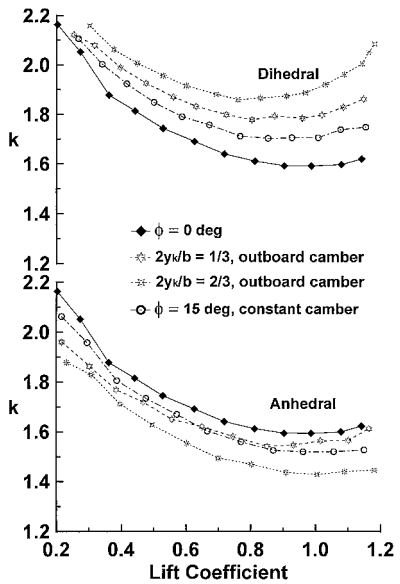

Fig. 6 Effect of outboard camber on induced efficiency.

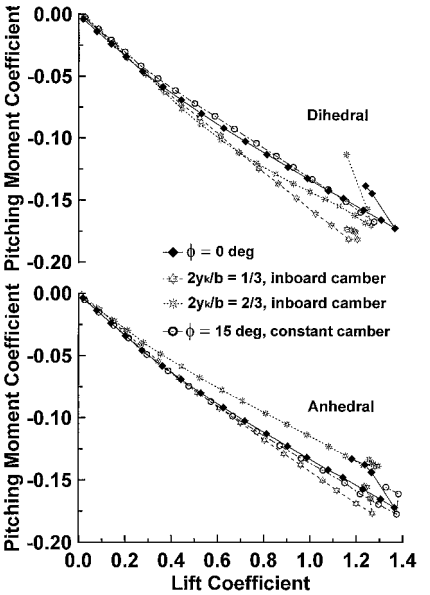

Fig. 7 Effect of inboard camber on measured pitching moment coefficient.

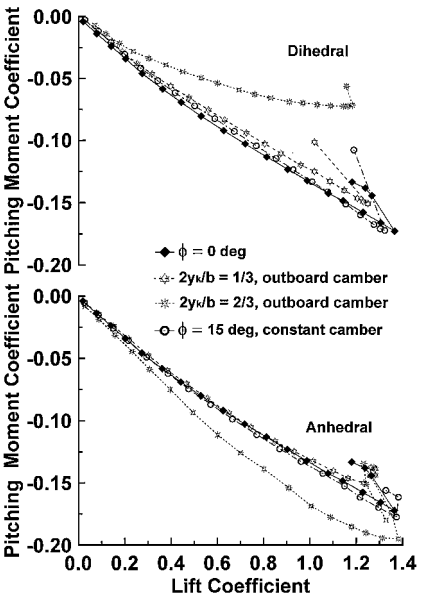

Fig. 8 Effect of outboard camber on measured pitching moment coefficient.

moment curve) is seen to be present at lower C_L for dihedral and for some of the anhedral cases than for the planar wing. Pitchup is usually associated with either vortex breakdown or tip separation/stall depending on the wing planform and leading-edge profile. For the present class of wings, pitchup is caused by vortex breakdown. This is a result of a loss of suction under the burst vortex as break down (BD) progresses from the wing trailing edge to the apex. Note that pitchup is coincident with $C_{L\,\max}$, indicating that the onset of BD at the wing trailing edge is coincident with a significant loss of lift at the trailing-edge region of the wing.

The effect of anhedral and dihedral for constant ϕ (i.e., a $\wedge$ or $\vee$ wing) on pitching moment is seen to be relatively minimal. This suggests that for this wing sweep, modifications to the wing flowfield by either anhedral or dihedral are effected uniformly such that the altered loading follows the load distribution of the projected planar wing. For inboard and outboard camber, this is not the case. For inboard camber, $2y_k/b = \frac{1}{3}$ shows a greater nose down moment for $C_L > 0.7$ for both anhedral and dihedral than the constant camber or planar wing. It is probable that the large inboard anhedral/dihedral angle (38.8 deg) significantly attenuates loading over the apex region of the wing, resulting in increased nose down moment. For inboard camber with $2y_k/b = \frac{2}{3}$, anhedral decreases nose down moment and dihedral increases nose down moment relative to the planar and constant camber wing, indicating that for this configuration inboard camber (dihedral) results in decreased loading over the wing apex region and vice versa. Outboard camber (Fig. 8) with $2y_k/b = \frac{2}{3}$ has a marked effect on pitching characteristics. Anhedral in this case has the opposite effect to that seen for inboard camber (Fig. 7) with a significant increase in nose down moment evident. The opposite is seen to be true for dihedral. Evidently the flowfield is extremely receptive to outboard camber with the kink located at $2y_k/b = \frac{2}{3}$. This form of camber significantly increases or decreases (anhedral or dihedral) loading aft, either through a localized increase of vortex strength and/or altered trajectory, as will be discussed later. Note that for $2y_k/b = \frac{1}{3}$, outboard camber has a very moderate effect on C_m.

Effects of spanwise camber on the location of the wing aerodynamic center (a.c.) are presented in Figs. 9 and 10. Generally, for full-span dihedral or anhedral, $\phi = \pm 15$ deg, the effect on the a.c. location is weak. This is in line with the prior discussion regarding the uniform chordwise modification to loading. Note that in all instances the a.c. moves forward toward the wing apex with increasing α.

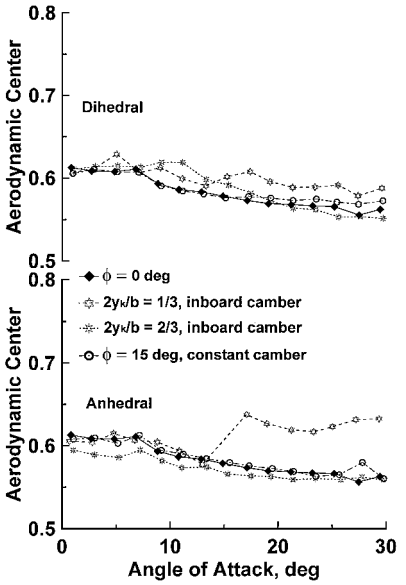

Fig. 9 Effect of inboard camber on location of the wing a.c.

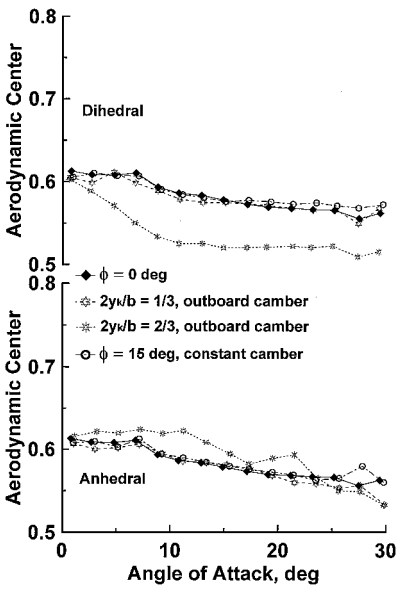

Fig. 10 Effect of outboard camber on location of the wing a.c.

This is due to increasing trailing-edge influence and, thus, departure from conical flow penetrating further upstream with elevated angle of attack. Kirkpatrick[23] has shown that the trailing-edge effects influence the vortex lift to a greater degree than the potential lift. Consequently, as the vortex lift constitutes an increasingly greater percentage of the total lift as α increases, the a.c. moves forward.

Inboard and outboard camber (Figs. 9 and 10) have a pronounced impact on the a.c. location, which would follow from their discontinuous planforms. Inboard camber with dihedral (see Fig. 9) clearly shows that the increase in negative pitching moment (see Fig. 7) is accompanied by a rearward shift in the a.c. location. This is most marked for $2y_k/b = \frac{1}{3}$ where the inner dihedral angle is 38.8 deg, which would unload the apex, moving the a.c. rearwards. For anhedral (Figs. 7 and 9), with $2y_k/b = \frac{2}{3}$, the pitching moment is less negative compared to the other shown configurations, indicating increased loading toward the apex as shown in Fig. 9 where the a.c. has moved forward. For this case, the effect of the inboard anhedral (inboard angle $= -21.9$ deg) is to enhance loading over the forward part of the wing. For $2y_k/b = \frac{1}{3}$, as seen for the dihedral case, pitching moment is more negative than for the other comparative configurations. Once again, the excessive (38.8-deg) inboard anhedral angle results in reduced loading forward on the wing with a commensurate rearward a.c. shift. The effect is seen to be more sporadic and pronounced for the $2y_k/b = \frac{1}{3}$ anhedral wing than for the dihedral wing. As will be shown later using on surface flow visualization, this configuration ($2y_k/b = \frac{1}{3}$) results in the formation of two distinct leading-edge vortices: one from the cambered inner panel and the other from the planar outboard panel. The distinct rearward shift in the a.c. location for $2y_k/b = \frac{1}{3}$ inboard anhedral may, thus, be due to the formation of a separate and distinct vortex on the planar outer wing panel at $\alpha \approx 14$ deg.

Outboard camber (Fig. 10) also displays a marked effect on the a.c. location, specifically for $2y_k/b = \frac{2}{3}$. For $2y_k/b = \frac{1}{3}$, there seems to be no distinct effect on the net chordwise load distribution for dihedral and anhedral. Dihedral with $2y_k/b = \frac{2}{3}$ shows a significant reduction in nose down pitching moment, which is accompanied by a significant forward a.c. shift. Evidently, this implementation of nonplanarity significantly attenuates loading aft. Similarly, anhedral for $2y_k/b = \frac{2}{3}$ leads to a significant increase in nose down pitching moment with a concomitant rearward shift of the wing's a.c. Presumably, the outboard anhedral increases loading aft, either through vortex manipulation or modification or through altering the trailing-edge pressure field.

The lift of delta wings is typically decomposed into two components, namely, vortex lift and potential or attached flow lift with zero leading-edge suction. An alternative decomposition is to separate lift into its linear and nonlinear components. The linear component is the attached flow lift component with the full attainable leading-edge thrust for the configuration, and is given by $k_P\alpha$. The nonlinear lift is then found as the difference of the total lift and the linear lift, that is, $C_L - k_P\alpha$. For a sharp-edged delta wing this decomposition, common in slender-wing theory, would result in a certain amount of the vortex lift being included with the linear lift component as the wing is physically not capable of generating leading-edge suction. Nonetheless, the linear and nonlinear lift separation has been used successfully by Kirby and Kirkpatrick[24] to decompose lift and pitching moment to allow the determination of the point of action of the linear and nonlinear lift components. The linear lift and pitching moment component is found by considering data points close to $\alpha = 0$ deg to establish the variation of lift with α and pitching moment with lift. It is, thus, implied that at these low α the generated lift does not contain any vortex effects. Following this methodology, lift and pitching moment were decomposed to determine their respective points of action, that is, their respective a.c. locations. Figure 11 shows the respective a.c. locations for $\Lambda_{pr} = 75$ deg and

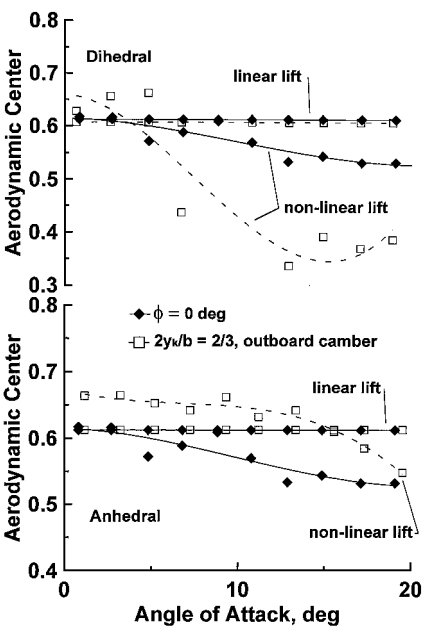

Fig. 11 Effect of outboard camber on the linear and nonlinear components of the wing's a.c.

$2y_k/b = \frac{2}{3}$ with outboard camber. Note that increasing α results in a forward movement of vortex induced loading. The same trends have been noted by Kirby.[25] It follows, as mentioned by Kirpatrick[23] and Kirby,[25] that trailing-edge effects are most significant in reducing the nonlinear lift component. Outboard camber effects are seen to be insignificant on the linear lift component. This form of nonplanarity has, however, a dramatic effect on the point of action of the nonlinear lift. For anhedral, the spanwise camber shifts the nonlinear a.c. rearwards, suggesting greater vortex induced loading toward the wing's trailing edge. This may be due to this form of nonplanarity drawing the vortex closer to the surface, augmenting the local vortex strength or effective induced loading as mentioned earlier. As the seven-hole probe data will subsequently show, outboard anhedral for this configuration locally increases the vortex strength while the vortex is still located above the planar wing panel, resulting in a significant localized increase of the vortex lift. The secondary separation vortex for this wing is also considerably stronger than that seen for any other configuration, further augmenting lift. Dihedral moves the nonlinear a.c. forward markedly, implying significantly reduced aft loading.

Results from the seven-hole probe surveys are presented in Figs. 12–16. The data were acquired at $U = 20$ m/s (giving a root chord $Re = 0.5 \times 10^6$) and $\alpha = 20$ deg. It was necessary to determine if the presence of the probe over the upper wing surface may have, in certain cases, precipitated the onset of BD. Payne[26] has shown that the presence of a probe can affect the location of vortex burst, particularly when the burst is near the wing's trailing edge. However, when the probe is not in close proximity to the burst location its influence is minimal.[26] It will be shown subsequently through vortex burst trajectories at $\alpha = 20$ deg that BD was not present over the wing. It is, thus, unlikely that the probe precipitated vortex bursting in any of the flow surveys.

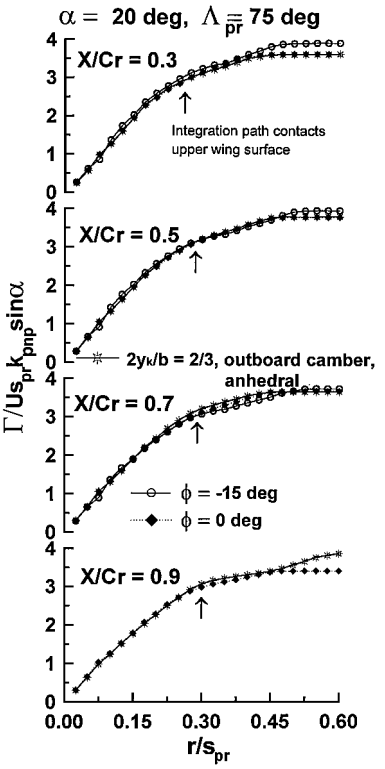

Fig. 14 Effect of outboard camber on the radial distribution of vortex circulation.

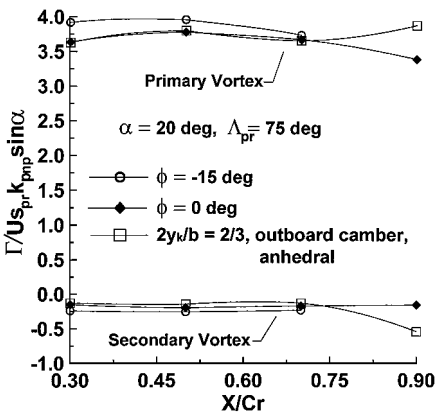

Fig. 12 Effect of outboard camber on the maximum vortex circulation; data reduced by projected semispan.

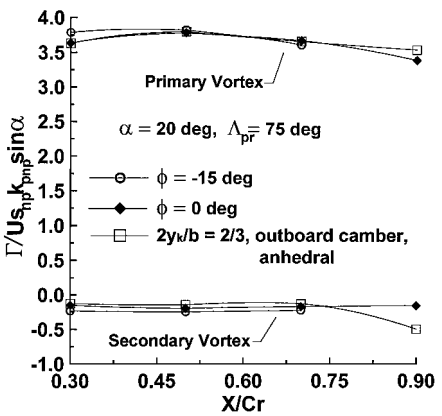

Fig. 13 Effect of outboard camber on the maximum vortex circulation; data reduced by nonplanar semispan.

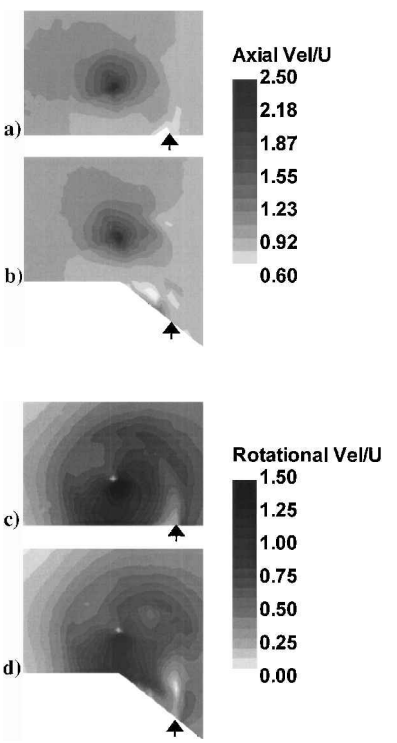

Fig. 15 Effect of outboard camber ($2y_k/b = \frac{2}{3}$) on vortex axial and rotational velocities, $x/c_r = 0.9$; arrow indicates leading edge: a) ϕ = 0 deg, b) ϕ = outboard anhedral, c) ϕ = 0 deg, and d) ϕ = outboard anhedral.

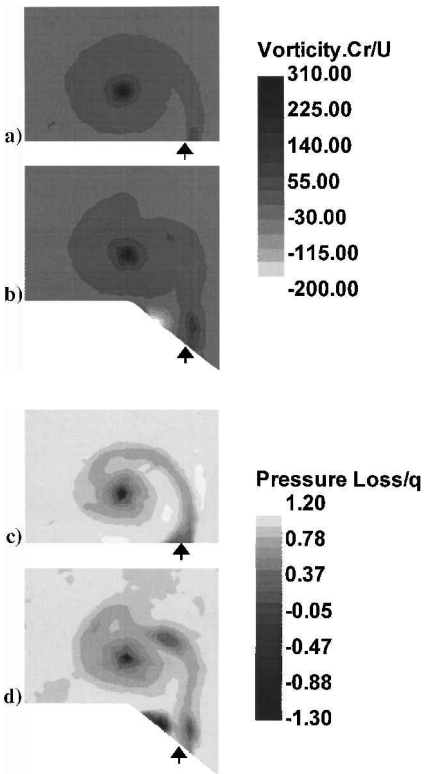

Fig. 16 Effect of outboard camber ($2y_k/b = \frac{2}{3}$) on vortex axial vorticity and pressure loss, $x/c_r = 0.9$; arrow indicates leading edge: a) $\phi = 0$ deg, b) ϕ = outboard anhedral, c) $\phi = 0$ deg, and d) ϕ = outboard anhedral.

Circulation was calculated using both the spatially integrated vorticity field and the crossflow velocity components. As the two methods showed excellent agreement, all radial circulation distributions were calculated through vorticity integration. The integrations proceeded from the vortex core center, that is, $r = 0$ to $r/s = 0.6$ in $\Delta(r/s) = 0.025$ intervals. The integration path for each r/s value was circular. When the integration path impinged on the upper wing surface, the wing was taken as the lower integration path and similarly for the edges of the survey grid. In Ref. 2, expressions are derived that relate the vortex strength to the wing's α as well as the attached flow wing lift curve slope k_p. It is shown that the vortex strength is proportional to k_p and $\sin\alpha$, whereas its chordwise growth is very nearly conical, that is, proportional to the local semispan. Consequently, to aid in interpretation, plots depicting circulation have been non dimensionalized primarily by $s_{\text{pr}} U k_{P\text{np}} \sin\alpha$, where $k_{P\text{np}}$ is the lift curve slope of the nonplanar wing. To establish the conical nature of the flowfield the reference length used to nondimensionalize the majority of the data is the projected semispan s_{pr} unless indicated otherwise. The maximum positive and negative circulation for the planar, $\phi = -15$ deg, and the outboard anhedral wing, $2y_k/b = \frac{2}{3}$, is presented in Fig. 12. The data show that Γ increases in a relatively conical or linear fashion for both the primary and secondary vortices, although a deviation near the trailing edge due to the Kutta condition is present for the planar wing. The outboard camber has virtually no impact on vortical development upstream of the kink, that is, $x/c_r \leq \frac{2}{3}$. For $x/c_r = 0.9$, however, the vortex circulation increases markedly for outboard camber such that, even excluding trailing-edge effects, Γ is greater than what would be expected assuming conical flow, that is, $\Gamma \propto s$. The secondary vortex also shows a substantial increase in circulation. Note that this vortex may be a new vortex that is formed at the spanwise kink, or may be an extension of the upstream secondary separation vortex or a coalescence of both. The increase of primary and secondary vortex circulation contributes to a localized increase in lift and, as a result, to the marked increase in nose down pitching moment mentioned earlier. As will also be discussed later, a large part of the leading-edge vortex for the outboard cambered wing is located above the planar inboard panel. Thus, the lift component of the induced loading is not reduced by $\cos\phi$, as is the case for constant anhedral or dihedral. To see if the increase in circulation of the outboard cambered section related to the increase in the semispan arc length, the data in Fig. 12 were reduced by the local nonplanar wing semispan. The result, shown in Fig. 13, is illuminating. It would appear the increase in total vortex strength for both the constant anhedral $\phi = -15$ deg and the outboard cambered wing compared to the planar wing is proportional to the actual length of the wing semispan. This is not the case for the strength of the kink (or secondary) vortex. This is not unexpected, however, as the secondary vortices formation is dominated by viscous effects.

The radial development of circulation for the three configurations, $\phi = 0$, -15 deg, and outboard camber $2y_k/b = \frac{2}{3}$ anhedral, is presented in Fig. 14. The initial radial development of circulation with r is relatively linear due to the addition of axis-symmetric vorticity located around the core. The reduction in the rate of increase of Γ with r ($r/s_{\text{pr}} > 0.2$) is a consequence of additional vorticity residing only in the leading-edge shear layer. Over the forward part of the wing, $x/c_r = 0.3$, $\phi = -15$ deg shows an increase in vortex strength over the radius of the vortex compared to the other wings. The increase in Γ is most noticeable near the wing leading edge, that is, $r/s_{\text{pr}} > 0.45$. For $x/c_r = 0.5$, all three configurations have similar circulation distributions, except for $\phi = -15$ deg near the wing leading edge, that is, large r/s_{pr}. It would be expected that an increase in shear layer circulation near the wing's leading edge would not greatly influence vortex-induced surface velocities and associated pressures. The outboard camber is seen to have an almost immediate effect relative to its chordwise location on the vortex strength, with a moderate increase in circulation compared to the other configurations evident for $r/s_{\text{pr}} > 0.25$ and $x/c_r = 0.7$. Near the trailing edge, $x/c_r = 0.9$, the outboard cambered configuration shows a marked increase in circulation compared to the planar wing with the majority of the incremental circulation present in the outboard extremity of the leading-edge shear layer. Note that for all plots in Fig. 14, the effects of the outboard camber are confined to the outer region of the vortex. This would be expected as the vortex filaments that ultimately constitute the vortex circulation follow a helical cylindrical path as they convect downstream, with each sequential strip of leading edge propagating a cylinder comprised of vortex filaments that enclose those convected downstream from the previous strip of the leading edge.[27]

The effects on vortex velocity, pressure loss, and vorticity of outboard anhedral camber for $2y_k/b = \frac{2}{3}$ are presented in Figs. 15 and 16. The displayed data were acquired at $x/c_r = 0.9$; comparative results for this axial location are also included for the planar wing. See Table 1 for a summary of vortex properties at this station. The outboard camber is seen to produce the maximum of axial vortex velocity with the core located farther outboard than for the planar wing, as may be seen in Figs. 15a and 15b. For both wings, the secondary vortex is clearly visible due to its wake-type axial flow. Note for the outboard cambered wing that a small cell of low velocity is located slightly outboard of the secondary vortex. Crossflow rotational velocity contours are presented in Figs. 15c and 15d. Note that the region of highest rotational velocity is distinctly asymmetric with respect to the core center (indicated by the white dot, signifying low rotational velocity). The rotational velocity maxima is located somewhat below and to the right of the vortex core due to lateral flow acceleration through the channel formed between the vortex and the wing. The rotational velocity profiles, Figs. 15c and 15d,

Table 1 Effects of outboard camber, $2y_k/b = \frac{2}{3}$, anhedral, on vortex aerodynamic parameters, $x/c_r = 0.9$ and $\alpha = 20$ deg

Λ_{pr}, deg	ϕ, deg	$\omega_{\min} c_r/U$	$\omega_{\max} c_r/U$	C_{pt}	$V_{\theta\max}/U$	$V_{A\min}/U$	$V_{A\max}/U$
75	0	−29.4	303.6	−1.29	1.46	0.64	2.38
75	−38.8	−197.7	307.2	−1.20	1.43	0.65	2.44

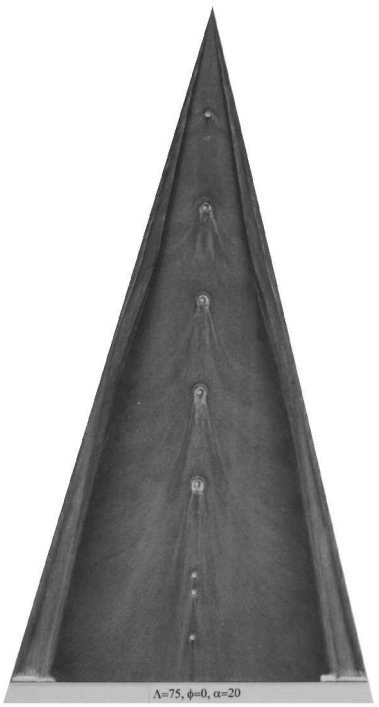

a) Planar wing

c) Outboard camber, anhedral, $2y_k/b = \frac{2}{3}$

e) Inboard camber, anhedral, $2y_k/b = \frac{1}{3}$

b) Constant anhedral wing, $\phi = -15$ deg

d) Outboard camber, anhedral, $2y_k/b = \frac{1}{3}$

f) Inboard camber, anhedral, $2y_k/b = \frac{2}{3}$

Fig. 17 Effect of spanwise camber on limiting streamline pattern, $\alpha = 20$ deg.

show that a lateral spanwise jet of significant rotational velocity is present just to the right of the kink (Fig. 15d) due to imposed velocities from both the primary and secondary vortices. Note that the rotational velocity peak is located farther to the right of the core for the planar than for the outboard cambered wing. This suggests that the secondary vortex is responsible for the measured lateral displacement of the rotational velocity peak relative to the vortex core, as consideration of the vortex location suggests a lessened influence of this vortex for the outboard cambered wing.

Figure 16 presents contours of pressure loss and vorticity. Pressure loss was defined as the difference between the local stagnation pressure and the freestream static pressure. The plots indicate that the secondary vortex of the cambered wing contains significant levels of vorticity; almost 65% of that of the primary vortex. The substructures present in the shear layer of the cambered wing, visible as areas of localized large pressure loss and increased vorticity, have been documented.[28] These vortical structures are spatially fixed, albeit convecting along a fixed helical path. It may also be seen that the shear layer of the cambered wing is distorted and somewhat rectangular in shape. The cambered wing's secondary vortex (dark region adjacent to the kink, Fig. 16d), which is clearly distinguishable from the leading-edge shear layer, is associated with a significant pressure loss. Comparison of Figs. 15b and 15d suggests that the substructures convect axially somewhat slower than the shear layer in which they are imbedded.

Limiting streamline (or skin-friction lines) patterns were established using titanium dioxide suspended in kerosene at $Re = 0.95 \times 10^6$ based on c_r. Surface flows for various inboard and outboard camber variations, as well as the planar wing, are presented. The limiting streamlines are indicative of the orientation of the surface shear stress or skin friction. Squire[29] conducted a theoretical study of the flow of a thin oil sheet under the boundary layer on a body. His results show that the oil flows in the direction of the surface shear, except near points of separation, where the oil tends to indicate separation prematurely. This is a consequence of the oil flow velocity tending to zero before the surface skin friction tends to zero. These results are largely independent of oil viscosity.[29] Squire also concluded that the effect of the oil on the boundary-layer motion is marginal. Furthermore, it is suggested that pressure gradients have an insignificant effect on the oil flow direction except near regions of separation, that is, in areas where the skin friction is small.

Figure 17a shows the typical footprint of the vortex-dominated flow over a delta wing. A strong vortex sidewash pattern, culminating in a secondary separation line, is present. Near the wing apex, a tertiary separation line is seen, indicating the presence of a tertiary vortex. At this α, axially attached flow constitutes a narrow wedge situated along the wing centerline. Transition of the crossflow boundary layer is indicated by the inflection in the secondary separation line at $x/c_r \approx 0.4$. Constant anhedral, $\phi = -15$ deg, shows a similar surface flowfield as the planar wing (see Figs. 17a and 17b). The flow disturbances present at the wing centerline are caused by the wing-mount anchoring holes.

Figure 17c presents the limiting streamline pattern over the outboard cambered, $2y_k/b = \frac{2}{3}$, anhedral, delta wing at $\alpha = 20$ deg. Comparison of Figs. 17a and 17c shows negligible variation in the flowfield upstream of the spanwise kink at $2y_k/b = \frac{2}{3}$, as would be expected if the circulation profiles are considered (Fig. 14). Downstream of the kink origin ($x/c_r > \frac{2}{3}$) Figs. 17a and 17c show that a sizeable part of the vortex footprint is still located above the planar portion of the wing. Thus, although the vortex strength is enhanced by the outboard camber (see Fig. 14), the vortex-induced suction acts largely on a planar surface. Therefore, unlike for constant anhedral, the induced loading is not reduced by $\cos\phi$ when resolved into its lift component. Figure 17c shows a distinct arced line of separation (thin white line) on the anhedral panel laterally coincident with the secondary separation line on the planar part of the wing. A reattachment line may also be seen lying outboard of the separation line on the deflected panel. Closer inspection of the surface flow in Fig. 17c suggests that the kink precipitates crossflow separation leading to a new secondary vortex. The enhanced definition seen in the secondary flows for the outboard cambered wing (on the deflected panel) compared to the planar wing (Fig. 17a) also suggests augmented strength, which, as shown in Fig. 12, is greatly increased over the planar wing.

Figure 17d shows the effect of outboard camber, $2y_k/b = \frac{1}{3}$, anhedral, on the surface flow pattern. It is apparent that the spanwise camber has a profound effect, resulting in a complicated flowfield. Multiple curved separation lines are present, suggesting the presence of large spanwise pressure gradients. Downstream over the wing, the primary vortex expands over the kink, resulting in a lateral displacement of the line of separation. The separation line extending from the kink ($x/c_r = \frac{1}{3}$) downstream is either the continuation of the secondary separation line, or a separation line caused by the formation of a new secondary separation vortex from the kink. The original secondary vortex, generated upstream, probably coalesces with the new secondary vortex some distance downstream of the kink. Farther downstream, the skin-friction lines show evidence of a tertiary separation.

The effects of inboard camber and anhedral with $2y_k/b = \frac{1}{3}$ and $\frac{2}{3}$ are presented in Figs. 17e and 17f, respectively. The limiting streamlines show that the inboard ($2y_k/b = \frac{1}{3}$) application of this form of camber results in the formation of two distinct secondary separation lines; one over the apex region and the second near the leading edge on the planar outboard panel. This is clearly associated with the formation of two distinct leading-edge vortices: one from the nonplanar inboard panel and the other from the planar outboard panel, as is also seen in the flow over double delta wings. For $2y_k/b = \frac{2}{3}$ (Fig. 17f) the skin-friction lines appear relatively unaffected by the spanwise camber distribution.

The effects of spanwise camber on vortex burst trajectories are summarized in Fig. 18. The data were acquired at $Re = 0.15 \times 10^6$ based on c_r. The wings were carefully aligned to minimize burst asymmetry of the left- and right-hand side vortices. However, as asymmetry is extremely sensitive to yaw and roll, slight model imperfections are capable of instigating asymmetry. Consequently, all of the presented data represent an average of the left- and right-hand side vortex burst locations. Highly swept delta wings are also prone to a chordwise oscillation of the burst location. To moderate the impact of the oscillations on the results, the burst trajectories were recorded on video. The burst location was then subsequently averaged for each α. Nonetheless, the asymmetry and chordwise oscillations do introduce an uncertainty into the results. Thus, the plots have a conservative or worst-case uncertainty bound included; it is expected that the uncertainty is somewhat less than that indicated. Effects of the outboard anhedral, $2y_k/b = 2/3$, are explored in Fig. 18. Also included is a repeated data run for the planar wing and data for $\phi = -15$ deg. The data clearly indicate that within the experimental accuracy, the effects of constant anhedral on vortex burst are generally marginal. Outboard anhedral effects mainly impact near the wing trailing edge, where a slightly earlier burst is precipitated. The earlier breakdown is presumably due to an increase in vortex strength at this chordwise location or altered trailing-edge effects.

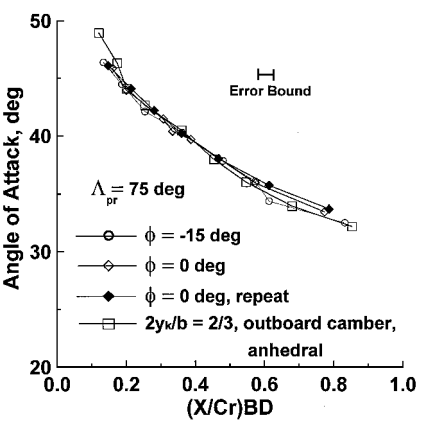

Fig. 18 Effect of outboard camber on vortex burst trajectory.

The repeatability of the planar wing's burst trajectories are seen to be satisfactory.

Conclusions

A wind-tunnel study was undertaken to determine the effect of various spanwise camber distributions on the aerodynamic characteristics of a 75-deg delta wing. The measurements include force balance data as well as a seven-hole probe survey and flow visualization results for the determination of vortex burst trajectories. From the study, the following conclusions are drawn:

Uniform as well as outboard camber can significantly augment lift, the implementation requiring only minor modifications to the planar wing geometry. For these configurations, anhedral generally produces lift augmentation compared to the basic wing, whereas dihedral has the opposite effect. As in the case of high AR, low-sweep wings, the wing modification is most effective for the wing forms studied when applied near the wing tips, generating lift through an increase in strength of both the primary and secondary wing leading-edge vortices. This outboard lift augmentation was associated with a marked increase in nose down pitching moment due to a rearward shift of the wing's aerodynamic center. Nonplanarity had a small effect on the vortex burst characteristics.

Acknowledgments

The author sincerely appreciates the insights offered by Murray Tobak of NASA Ames Research Center regarding interpretation of the skin-friction patterns on the outboard cambered wings. Thanks are also extended to the reviewers for their comments and suggestions.

References

[1]Winter, H., "Stromungsvorgange an Platten und Profilierten Korpern bei kleinen Spannweiten," *Forschung auf dem Gebiete des Ingenieur-Wesens*, Vol. 6, No. 2, 1935, pp. 67–71.

[2]Traub, L. W., "Prediction of Delta Wing Leading-Edge Vortex Circulation and Lift-Curve Slope," *Journal of Aircraft*, Vol. 34, No. 3, 1997, pp. 450–452.

[3]Rinoie, K., and Stollery, J. L., "Experimental Studies of Vortex Flaps and Vortex Plates; Part 2. 1.15 m Span 60° Delta Wing," National Aerospace Lab., TR-1180T, Tokyo, Oct. 1992.

[4]Traub, L. W., "Aerodynamic Characteristics of Vortex Flaps on a Double-Delta Planform," *Journal of Aircraft*, Vol. 32, No. 2, 1995, pp. 449, 450.

[5]Traub, L. W., "Effects of Spanwise Blowing on a Delta Wing with Vortex Flaps," *Journal of Aircraft*, Vol. 32, No. 4, 1995, pp. 884–887.

[6]Traub, L. W., and Galls, S., "Effects of Leading and Trailing Edge Gurney Flaps on a Delta Wing," *Journal of Aircraft*, Vol. 36, No. 4, 1999, pp. 651–658.

[7]Munk, M. M., "The Minimum Induced Drag of Aerofoils," NACA Rept. 121, 1921.

[8]Cone, C. D., "The Theory of Induced Lift and Minimum Induced Drag of Nonplanar Lifting Systems," NASA TR R-139, Feb. 1962.

[9]Lowson, M. V., "Minimum Induced Drag for Wings with Spanwise Camber," *Journal of Aircraft*, Vol. 27, No. 7, 1990, pp. 627–631.

[10]Fernandez, J., and Holla, V. S., "Spanwise Cambered Delta Wing with Leading Edge Separation," *Journal of Aircraft*, Vol. 14, No. 3, 1977, pp. 276–282.

[11]Squire, L. C., "Camber Effects on the Non Linear Lift of Slender Wings with Sharp Leading Edges," Aeronautical Research Council, CP 924, 1966.

[12]Queijo, M. J., and Jaquet, B. M., "Investigation of Effects of Geometric Dihedral on Low-Speed Static Stability and Yawing Characteristics of an Untapered 45 degree Sweptback-Wing Model of an Aspect Ratio 2.61," NACA TN 1668, Sept. 1948.

[13]Maggin, B., and Shanks, R. E., "The Effect of Geometric Dihedral on the Aerodynamic Characteristics of a 40 degree Swept-Back Wing of Aspect Ratio 3," NACA TN 1169, Dec. 1946.

[14]Washburn, K. E., and Gloss, B. B., "The Effects of Wing Dihedral and Section Suction Distribution on Vortex Bursting," NASA TM X-72745, July 1975.

[15]Washburn, K. E., and Gloss, B. B., "Effect of Wing-Tip Dihedral on the Longitudinal and Lateral Aerodynamic Characteristics of a Supersonic Cruise Configuration at Subsonic Speeds," NASA TM X-72693, Aug. 1976.

[16]Smith, L. A., and Campbell, R. L., "Effects of Winglets on the Drag of a Low-Aspect-Ratio Configuration," NASA TP-3563, Feb. 1996.

[17]Polhamus, E. C., "Prediction of Vortex-Lift Characteristics by a Leading Edge Suction Analogy," *Journal of Aircraft*, Vol. 8, No. 4, 1971, pp. 193–199.

[18]Traub, L. W., "Lift Prediction of Spanwise Cambered Delta Wings," *Journal of Aircraft*, Vol. 36, No. 3, 1999, pp. 515–522.

[19]Traub, L. W., "Effects of Anhedral and Dihedral on a 75-deg Sweep Delta Wing," *Journal of Aircraft*, Vol. 37, No. 2, 2000, pp. 302–312.

[20]Wentz, W. H., Jr., and Kohlman, D. L., "Vortex Breakdown on Slender Sharp-Edged Delta Wings," *Journal of Aircraft*, Vol. 8, No. 3, 1971, pp. 156–161.

[21]Pope, A., and Rae, W. H., *Low-Speed Wind Tunnel Testing*, Wiley, New York, 1984, pp. 199–208, 362–424.

[22]Shindo, S., "Simplified Tunnel Correction Method," *Journal of Aircraft*, Vol. 32, No. 4, 1995, pp. 210–213.

[23]Kirkpatrick, D. L. I., "Analysis of the Static Pressure Distribution on a Delta Wing in Subsonic Flow," Aeronautical Research Council, Research and Memoranda 3619, London, 1970.

[24]Kirby, D. A., and Kirkpatrick, D. L. I., "An Experimental Investigation of the Effect of Thickness on the Subsonic Longitudinal Stability Characteristics of Delta Wings of 70 deg Sweep-Back," Aeronautical Research Council, Research and Memoranda 3673, London, 1971.

[25]Kirby, D. A., "An Experimental Investigation of the Effect of Planform Shape on the Subsonic Longitudinal Stability Characteristics of Slender Wings," Aeronautical Research Council, Research and Memoranda 3568, London, 1969.

[26]Payne, F. M., "The Structure of Leading-Edge Vortex Flows Including Breakdown," Ph.D. Dissertation, Dept. of Aerospace and Mechanical Engineering, Univ. of Notre Dame, South Bend, IN, May 1987.

[27]Lowson, M. V., "Visualization Measurements of Vortex Flows," *Journal of Aircraft*, Vol. 28, No. 5, 1991, pp. 320–327.

[28]Washburn, A. E., "Effects of External Influences on Subsonic Delta Wing Vortices," AIAA Paper 92-4033, July 1992.

[29]Squire, L. C., "The Motion of a Thin Oil Sheet Under the Steady Boundary Layer on a Body," *Journal of Fluid Mechanics*, Vol. 11, Sept. 1961, pp. 161–179.